

Fast ejecta as a potential way to distinguish black holes from neutron stars in high-mass gravitational-wave events

ELIAS R. MOST ^{1,2,3}, L. JENS PAPENFORT ⁴, SAMUEL TOOTLE ⁴, AND LUCIANO REZZOLLA ^{4,5,6,7}

¹*Princeton Center for Theoretical Science, Princeton University, Princeton, NJ 08544, USA*

²*Princeton Gravity Initiative, Princeton University, Princeton, NJ 08544, USA*

³*School of Natural Sciences, Institute for Advanced Study, Princeton, NJ 08540, USA*

⁴*Institut für Theoretische Physik, Goethe Universität, Max-von-Laue-Str. 1, 60438 Frankfurt am Main, Germany*

⁵*School of Mathematics, Trinity College, Dublin 2, Ireland*

⁶*Frankfurt Institute for Advanced Studies, Ruth-Moufang-Str. 1, 60438 Frankfurt am Main, Germany*

⁷*Helmholtz Research Academy Hesse for FAIR, Max-von-Laue-Str. 12, 60438 Frankfurt am Main, Germany*

(Received December 8, 2020; Revised; Accepted)

ABSTRACT

High-mass gravitational-wave events in the neutron-star mass range, such as GW190425, have recently started to be detected by the LIGO/Virgo detectors. If the masses of the two binary components fall in the neutron-star mass range, such a system is typically classified as a binary neutron-star system, although the detected gravitational-wave signal may be too noisy to clearly establish a neutron-star nature of the high-mass component in the binary and rule out a black hole–neutron star system for such an event. We here show that high-mass binary neutron-star mergers with a very massive neutron-star primary close to the maximum-mass limit, $m_1 \gtrsim 2.2 M_\odot$, produce at merger fast dynamical mass ejecta from the spin-up of the primary star at merger. By simulating the merger of black hole–neutron star systems of exactly the same masses and spins, we show that these fast ejecta are entirely absent, if the primary is instead a black hole. In addition, we find that both systems leave almost identical amounts of baryon mass behind, which is not immediately accreted by the black hole. This implies that both systems will likely have comparable electromagnetic afterglow emission stemming from the remnant disk. Hence, fast ejecta at merger have the potential to distinguish neutron stars from black holes in high-mass mergers, although these ejecta may be challenging to detect observationally.

Keywords: gravitational waves — stars: neutron — black hole — neutron star mergers — binary neutron-star mergers

1. INTRODUCTION

Since the first detection of a multi-messenger gravitational event involving the merger of two neutron stars (NSs), GW170817 (Abbott et al. 2017), two additional gravitational-wave events, GW190425 (Abbott et al. 2020) and GW190814 (The LIGO Scientific Collaboration et al. 2020), have been detected where at least one of the binary components lies within the NS mass range. In the case of GW190814, which features a $23 M_\odot$ black hole (BH) and a $2.6 M_\odot$ companion, the nature of the secondary has not been determined and is

also at odds with our current understanding of compact binary system formation channels (Zevin et al. 2020; Hamers & Safarzadeh 2020; Safarzadeh & Loeb 2020; Mandel et al. 2020; Liu & Lai 2020; Lu et al. 2020). As a result, the secondary of GW190814 could either have been a BH (the lightest ever detected, but likely produced by the collapse of a NS) or a stable NS (the heaviest ever detected) (Most et al. 2020a; Tan et al. 2020; Zhang & Li 2020; Vattis et al. 2020; Fattoyev et al. 2020; Tsokaros et al. 2020; Godzieba et al. 2020; Essick & Landry 2020; Lim et al. 2020; Roupas 2020; Sedrakian et al. 2020; Tews et al. 2020; Biswas et al. 2020; Dexheimer et al. 2020; Cao et al. 2020; Kawaguchi et al. 2020). Conversely, GW190425 with a total mass of $3.4 M_\odot$ lies firmly in the NS mass range, i.e., with

individual masses being less than current constraints on the maximum mass of nonrotating NSs, M_{TOV} , either from gravitational-wave events (Margalit & Metzger 2017; Rezzolla et al. 2018; Ruiz et al. 2018; Shibata et al. 2019) or from pulsar observations (Cromartie et al. 2020; Antoniadis et al. 2013). Since no electromagnetic counterpart has been observed for either event (Coughlin et al. 2020; Vieira et al. 2020; Ackley et al. 2020; Watson et al. 2020; Dobie et al. 2019; Andreoni et al. 2020) and the tidal deformability constraints remain inconclusive (The LIGO Scientific Collaboration et al. 2020), a BH–NS as the source of this event cannot be fully ruled out (Foley et al. 2020; Kyutoku et al. 2020). This raises the general question of how the merger of two NSs can be distinguished from the merger of a NS and a BH when the gravitational-wave detection is not sufficiently accurate to place a lower bound on the tidal deformability of the system.

One potential avenue is to check for consistency of the masses with the allowed mass range for NSs (Foley et al. 2020; Most et al. 2020b), which is complicated by the degeneracy between the mass ratio and the effective spin in the gravitational-wave phase (Harry & Hinderer 2018). While the same arguments have been applied also to GW190814 (Most et al. 2020a; Zhang & Li 2020; Biswas et al. 2020), they have largely remained inconclusive and can provide deeper insights only if it was known a priori if the system contained either a NS or a BH primary.

Another possibility to constrain the nature of the system is through the use of optical counterparts, in particular through the kilonova afterglow (Metzger 2017). Numerical investigations have shown that BH–NS systems typically feature mass outflows that are different from those of NS–NS systems (e.g., Foucart 2012; Foucart et al. 2013; Kyutoku et al. 2015, 2018). The dynamical mass ejection in a BH–NS system will only stem from the unbound parts of a tidally disrupted NS (Rosswog 2005; Kyutoku et al. 2013, 2015), whereas NS–NS mergers will also feature a collision shock and mass ejection from the stable remnant (Baiotti et al. 2008; Foucart et al. 2016; Sekiguchi et al. 2015; Lehner et al. 2016; Bovard et al. 2017). Furthermore, the presence of a blue kilonova associated with shock heated ejecta coming from the surface of the remnant NS (Perego et al. 2016; Fujibayashi et al. 2017), is different to the predominantly red kilonova emission associated with the long-term mass ejection from the accretion disk (Fernández et al. 2015a,b; Siegel & Metzger 2017; Miller et al. 2019). Consistent with astrophysical expectations from population synthesis models, most numerical studies of BH–NS mergers have focussed on intermediate mass ratios

$q^{-1} := m_1/m_2 = 4 - 8$, where $m_{1,2}$ are the masses of the two binary components, (Etienne et al. 2009; Kyutoku et al. 2011, 2015; Foucart et al. 2012, 2013), with BHs outside of the anticipated mass gap (Kruckow et al. 2018). Using parameter ranges consistent with GW170817, Hinderer et al. (2019) have performed the first direct comparison of a NS–NS merger with a BH–NS merger. In these simulations they contrasted the evolution of a stable remnant NS with that of the accretion disk in the BH–NS case, in addition to tidal deformability constraints from the gravitational waveform. While they find that a BH–NS nature is difficult to reconcile with the EM counterparts of GW170817, it cannot be fully ruled out. Kyutoku et al. (2020) have focussed on the observational implications of a BH–NS in the GW190425 mass range, whereas Foucart et al. (2019); Hayashi et al. (2020) have performed general investigations of near equal-mass NS–NS mergers, studying in particular the mass ejection and remnant disk masses (Foucart et al. 2018).

One of the open problems in these studies remains the formation history of the low-mass BH in these binary systems. In fact, while forming BHs with $< 5 M_{\odot}$ remains very challenging (Zevin et al. 2020; Ertl et al. 2020), forming a BH with masses $m_{\text{BH}} < M_{\text{TOV}}$ remains even more challenging and typically involves invoking primordial BH formation (García-Bellido et al. 1996). Yet, recent observations provide a basis for assuming the formation of very heavy NSs (Cromartie et al. 2020) beyond the currently assumed galactic pulsar-mass distribution (Alsing et al. 2018; Tauris et al. 2017). Although overall less likely, if such a star had a massive companion, accretion induced collapse (Qin et al. 1998; Rueda & Ruffini 2012; Fryer et al. 2014), as suggested for Cyg X-3 (Zdziarski et al. 2013) or GRB090618 (Izzo et al. 2012), or removal of angular momentum, e.g., via pulsar spin-down (Falcke & Rezzolla 2014), of a very massive rotationally supported NS could lead to the formation of a BH with masses $m_{\text{BH}} \approx M_{\text{TOV}}$. Such systems are very interesting in the present context, because they do not only lie within the mass range of GW190425-like binaries, but they also represent a region of the mass range where NS–NS and BH–NS could potentially coexist. Making use of quasi-universal relations relating the mass ratio and the effective spin

$$\tilde{\chi} := \frac{m_1 \chi_1 + m_2 \chi_2}{m_2 + m_1} = \frac{\chi_1}{1+q} \left(1 + q \frac{\chi_2}{\chi_1} \right), \quad (1)$$

it is possible to perform targeted simulations aimed at identifying potential differences between BH–NS and NS–NS merger for GW190425-like events. We here present a comparison between BH–NS and NS–NS merg-

ers in the relevant parameter range, i.e., for mass ratios $q^{-1} \approx 2$ and primary spins $0 \leq \chi_1 \leq 0.53$.

This paper is structured as follows, in Sec. 2 we summarize the numerical methods used in this study. Section 3 presents a detailed comparison of the dynamical mass ejection of BH–NS and NS–NS mergers, and identifies a fast ejection signatures characteristic for NS–NS merger in this mass range. Finally, Sec. 4 concludes with a discussion of the impact of these results.

2. METHODS

To model the evolution of the compact binaries in full general relativity, we numerically solve the Einstein field equations using a constraint-damping formulation of these equations (Bernuzzi & Hilditch 2010; Alic et al. 2012) [in these specific simulations we have used the Z4c formulation of Hilditch (2013)], coupled to the equations of general-relativistic magnetohydrodynamics (GRMHD) (Duez et al. 2005; Shibata & Sekiguchi 2005; Giacomazzo & Rezzolla 2007) using the Frankfurt-/IllinoisGRMHD code (FIL) (Most et al. 2019b,a), which is derived from the IllinoisGRMHD code (Etienne et al. 2015), but implements high-order (fourth) conservative finite-difference methods (Del Zanna et al. 2007) and can handle temperature and electron-fraction dependent equations of state (EOSs). Neutrino cooling and weak interactions are included in the form of a neutrino leakage scheme (Ruffert et al. 1996; Rosswog & Liebendörfer 2003; Galeazzi et al. 2013).

FIL makes use of the Einstein Toolkit infrastructure (Löffler et al. 2012), and, in particular, of the adaptive mesh-refinement driver Carpet (Schnetter et al. 2004), which allows to decompose the numerical domain in a box-in-box approach. The simulations presented here make use of nine nested Cartesian boxes and a refinement ratio of two. The outermost box stretches to $\simeq 6000$ km in each direction and the innermost box covering the BH/primary NS and (initially) the NS extends to about 17.7 km with a finest resolution of $\simeq 215$ m. While we have included a buried dipolar magnetic field of $\simeq 10^{14}$ G in the secondary. For consistency with the BH–NS data set, where the primary is a BH, we have not included a magnetic field in the primary NS of the NS–NS system. We find that their presence does not influence the dynamics and mass ejection at merger. Rather, magnetic fields will affect the post-merger evolution of the remnant accretion disk (see, e.g., Giacomazzo et al. 2011; Dionysopoulou et al. 2015), which we will present in a separate study.

We model the initial binary configurations via the solution of the Einstein constraint equations for either BH–NS (Taniguchi et al. 2005; Grandclément 2006;

Taniguchi et al. 2007), or NS–NS (Tichy 2012; Tacik et al. 2015; Tsokaros et al. 2015; Papenfort et al. 2020) binaries. More specifically, the initial data is constructed in the extended conformal thin-sandwich (XCTS) formalism (Pfeiffer & York 2003; Pfeiffer & York 2005). In the case of BH–NS binaries, the BH is modelled using excision boundary conditions (Grandclément 2006), imposing the spin via a shift condition on the horizon (Caudill et al. 2006). The secondary NS, on the other hand, is assumed to be irrotational. The initial data is constructed using the publicly available LORENE code (Grandclément 2006). On import onto the Cartesian domain, the excised interior of the BH is filled using simple eight-order extrapolation (Etienne et al. 2007; Etienne et al. 2009). In the case of NS–NS binaries, instead, the spinning NS is constructed following the formalism proposed by Tichy (2012), for which the velocity field of the star is a combination of an irrotational and of a uniformly rotating part. The initial data is then computed using the Kadath spectral library (Grandclément 2010), which has recently been extended for compact binary initial data (Papenfort et al. 2020). In this way, we are able to generate NS–NS initial data involving supramassive NSs with masses exceeding M_{TOV} and supported by the additional angular momentum. We model the microphysical composition of the NS and finite-temperature effects in the merger using an EOS with realistic nuclear forces (Togashi et al. 2017), hereafter referred to as TNTYST. We also perform simulations using an EOS containing hyperons (Banik et al. 2014), which is based on the DD2 EOS (Hempel & Schaffner-Bielich 2010), and referred to as BHBA Φ . With a maximum mass of $M_{\text{TOV}} = 2.22$ (2.10) M_{\odot} and a radius of $R_{1.4} = 11.54$ (13.22) km for a 1.4 M_{\odot} NS for the TNTYST (BHBA Φ) EOS, we can cover a range of maximum masses (Margalit & Metzger 2017; Rezzolla et al. 2018; Ruiz et al. 2018; Shibata et al. 2019) and radii (Annala et al. 2018; Most et al. 2018; De et al. 2018; Abbott et al. 2018) that are consistent with GW170817 (Abbott et al. 2017; The LIGO Scientific Collaboration et al. 2017).

Our attention here is particularly focused on the potential differences between NS–NS and BH–NS mergers in the near equal-mass regime. Inspired by the detection of GW190425 with a total mass $M = 3.4_{-0.1}^{+0.3} M_{\odot}$, we adopt a total mass of $M = 3.6 M_{\odot}$ for our binary systems. This guarantees that even when considering small mass ratios of $q^{-1} \approx 2$, the secondary mass $m_2 = qM / (1 + q) > 1.17 M_{\odot}$, which is consistent with the proposed lower bounds on the NS mass (Suwa et al. 2018). Assuming that no BHs are likely to be formed with masses $M_{\text{BH}} < M_{\text{TOV}}$, we focus on the limiting

Table 1. Summary of the properties of the initial binaries. The columns list: the dimensionless spin χ_1 of the primary, the effective spin $\tilde{\chi} = \chi_1/(1+q)$, the mass ratio $q = m_2/m_1$ and the individual (baryon) masses of the primary, $m_{(b),1}$, and of the secondary, $m_{(b),2}$. All binaries have a total mass $M_{\text{ADM}} = 3.6 M_\odot$ and are at an initial separation of 45 km. The secondary is always non-spinning, $\chi_2 = 0$.

	$m_1 [M_\odot]$	$m_2 [M_\odot]$	$m_{b,1} [M_\odot]$	$m_{b,2} [M_\odot]$	q	χ_1	$\tilde{\chi}$	EOS
TNT.BH.chit.0.00	2.20	1.40	–	1.55	0.636	0.00	0.00	TNTYST
TNT.BH.chit.0.15	2.24	1.36	–	1.50	0.608	0.24	0.15	TNTYST
TNT.BH.chit.0.35	2.42	1.18	–	1.28	0.486	0.52	0.35	TNTYST
TNT.NS.chit.0.00	2.20	1.40	2.66	1.55	0.636	0.00	0.00	TNTYST
TNT.NS.chit.0.15	2.24	1.36	2.70	1.50	0.608	0.24	0.15	TNTYST
TNT.NS.chit.0.35	2.42	1.18	2.87	1.28	0.486	0.52	0.35	TNTYST
BHBLP.BH.chit.0.00	2.10	1.50	–	1.65	0.636	0.00	0.00	BHBA Φ
BHBLP.BH.chit.0.15	2.14	1.46	–	1.60	0.608	0.24	0.15	BHBA Φ
BHBLP.NS.chit.0.00	2.20	1.40	2.40	1.65	0.636	0.00	0.00	BHBA Φ
BHBLP.NS.chit.0.15	2.24	1.36	2.48	1.60	0.608	0.24	0.15	BHBA Φ

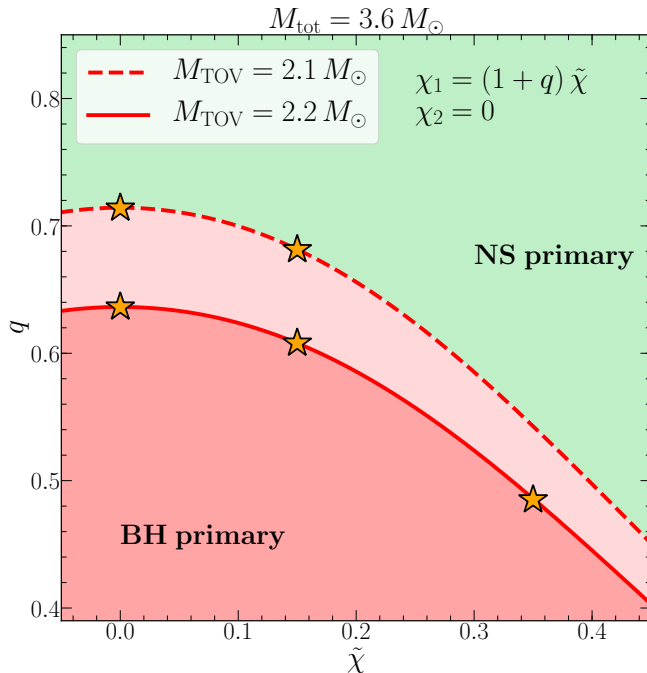


Figure 1. Schematic overview of the allowed area (green) and the excluded area (red) for the masses in NS-NS systems. The solid and dashed red lines are computed for a spin distribution, $\chi_1 = (1+q)\tilde{\chi}$ and $\chi_2 = 0$, in terms of the effective spin $\tilde{\chi}$, mass ratio q and total mass M_{tot} . Assuming $M_{\text{BH}} \simeq M_{\text{TOV}}$, the red lines outline a region for which is potentially shared by NS-NS and BH-NS binaries.

value of $M_{\text{BH}} \simeq M_{\text{TOV}}$, which would model a BH-NS system derived from NS-NS binary where the BH is produced by means of a continued mass accretion (Safarzadeh & Loeb 2020). NSs in this mass range either have to be nonrotating and have masses below M_{TOV} , or

be rapidly rotating if they have larger masses but still $\lesssim 1.2 M_{\text{TOV}}$ (Breu & Rezzolla 2016). For fixed M_{TOV} , the threshold configuration for such a NS-NS system can be computed using quasi-universal relations (Most et al. 2020b). Following Most et al. (2020b), we adopt three fiducial effective spin parameters $M\tilde{\chi} = m_1\chi_1 + m_2\chi_2$, where m_i and χ_i are the individual spins of the two binary components. We further assume that the primary reached its high mass by accretion from the progenitor star of the secondary, and, thus, also received additional angular momentum (Tauris et al. 2017). For this reason, we find it reasonable to assume that the primary spins much faster than the secondary, i.e.,

$$\chi_1 \gg \chi_2 \approx 0, \quad (2)$$

which leads to [cf., Eq. (1)]

$$\tilde{\chi} \approx \chi_1 / (1+q). \quad (3)$$

We then choose $\tilde{\chi} = [0.00, 0.15, 0.35]$, which corresponds to primary masses $m_1 = [2.20, 2.24, 2.42] M_\odot$, mass ratios $q = [0.636, 0.608, 0.486]$ and primary spins $\chi_1 = [0.00, 0.24, 0.52]$ for the TNTYST EOS. For the BHBA Φ EOS we instead use $\tilde{\chi} = [0.00, 0.15]$ ¹, which corresponds to primary masses $m_1 = [2.1, 2.14] M_\odot$, mass ratios $q = [0.714, 0.681]$, and primary spins $\chi_1 = [0.00, 0.25]$. The properties of the simulated components in the bi-

¹ We have not included models with spins $\tilde{\chi} = 0.35$ for the BHBA Φ EOS, since the initial data could would always converge to a solution for which the primary lies on the dynamically unstable branch. This issue will be addressed in a future release of the initial data code (Papenfort et al. 2020).

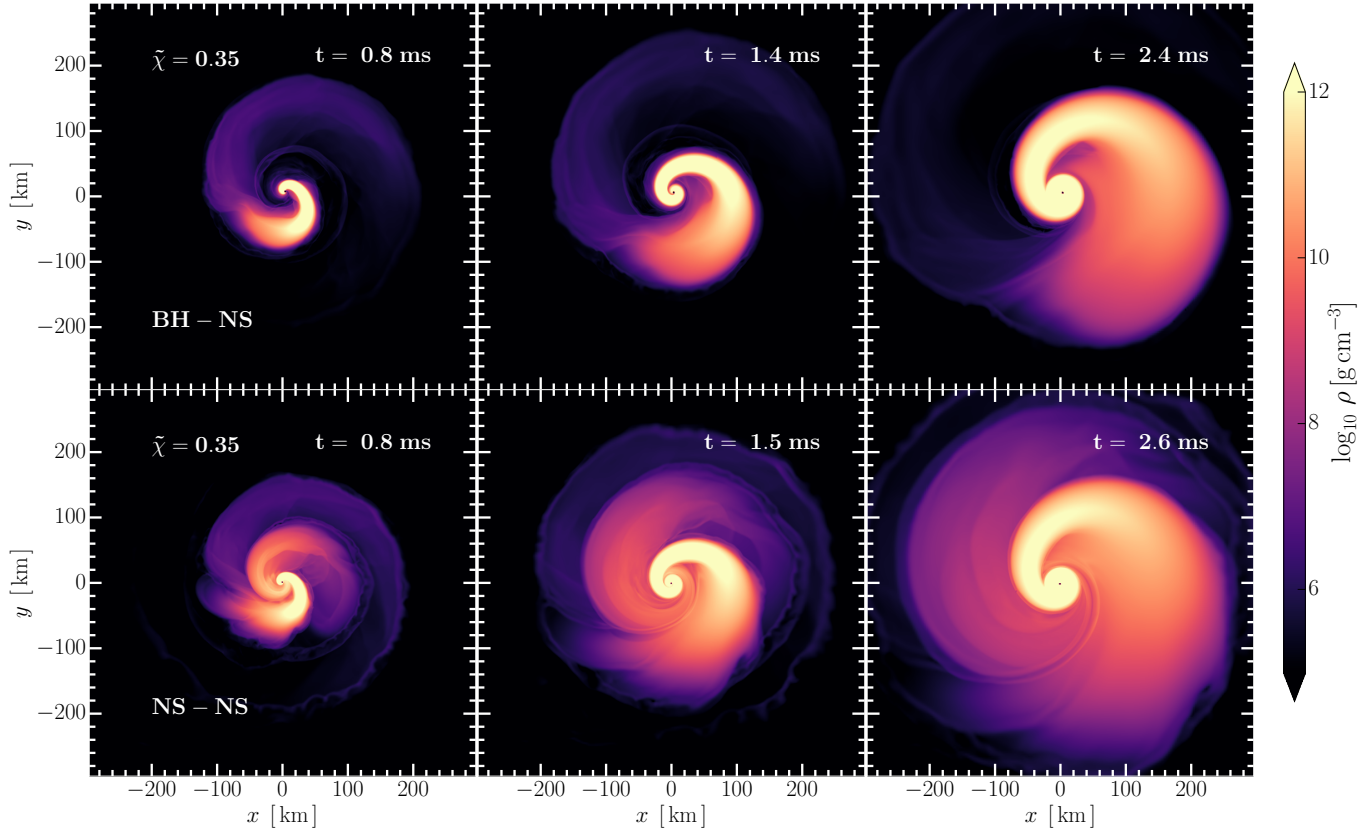


Figure 2. Tidal disruption for high-mass NS–NS (bottom) and BH–NS mergers (top) for effective spin $\tilde{\chi} = 0.35$, computed using the TNTYST EOS. Shown are three different times at merger. The NS–NS merger clearly features a second mass-ejection arm.

naries are collected in Table 1 and their position in the $(q, \tilde{\chi})$ plane is marked with stars in Fig. 1.

3. RESULTS

In the following we present the results of our simulations. In particular, we compare the evolution of NS–NS systems to that of BH–NS systems with the exact same mass configuration, concentrating on the cases in which the mass of the primary is very close either to the maximum mass of nonrotating configurations (i.e., $m_1 \simeq M_{\text{TOV}}$) or to the maximum mass of rotating configurations (i.e., $m_1 \simeq M_{\text{max}}(\chi_1)$).

3.1. Matter dynamics

We present the dynamics at merger in Fig. 2, which shows the baryonic rest-mass density ρ on the (x, y) plane for the high-spin system, $\tilde{\chi} = 0.35$, computed using the TNTYST EOS, where the top row shows the BH–NS merger and the bottom row the corresponding NS–NS merger at different times. The three images illustrate the behaviour within a time interval of 2 ms during the merger. Note that for the BH–NS system (top row), the NS is tidally disrupted outside of the innermost stable circular orbit (ISCO) and the matter and

can thus form an accretion disk around the BH (Shibata & Taniguchi 2011). The long-term evolution of this disk is then able to account for a predominantly red kilonova signal (Fernández et al. 2015b; Siegel & Metzger 2017). Contrasting this behaviour with the evolution of a NS–NS system (bottom row), it is possible to note that the overall picture is remarkably similar (the snapshots are chosen so as to underline the analogies). Indeed, as first pointed out by Dietrich et al. (2017), the merger of two NSs at such high-mass ratios $q^{-1} \simeq 2$, results in an evolution similar to that of BH–NS systems. Despite the qualitative analogies between the BH–NS and NS–NS binaries in our simulations, we crucially, find that for NS–NS systems an additional arm of mass ejection rapidly emanating from the merger site (see also Fig. 7). By carefully studying the temporal evolution of the merger process (compare left, middle and right panels in the bottom row), we found that this additional mass ejection represents a second tidal tail, propagating in a direction that is opposite to that of the main tidal tail. This is very apparent when contrasting the two rightmost panels of Fig. 2, where it is clear that there is essentially no mass ejected in the negative x -direction in the case of the BH–NS binary (top right), while there is a

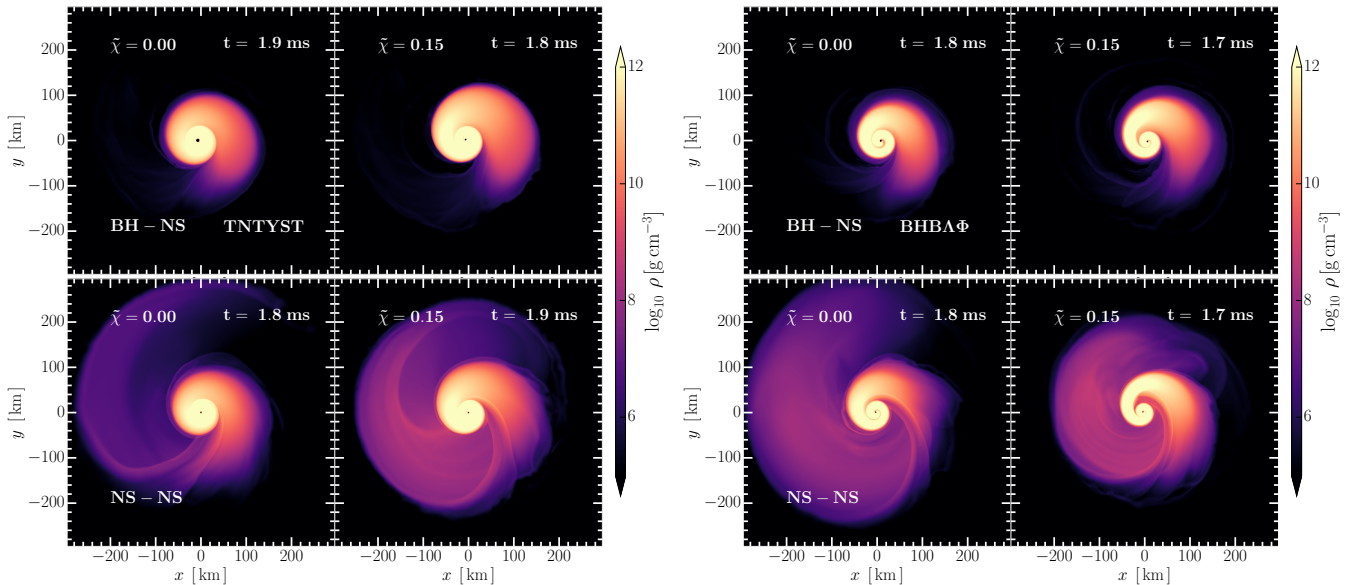


Figure 3. Same as Fig. 2 but for $\tilde{\chi} = 0.00$ and for $\tilde{\chi} = 0.15$. *Left:* Simulations using the TNTYST EOS. *Right:* Simulations using the BHBA Φ EOS.

large tidal tail in the case of the NS–NS binary (bottom right). Indeed, the left-moving tidal tail is comparable, albeit smaller, than the right-moving tail.

This different dynamical behaviour is due to the fact that in the NS–NS binary, the largest tidal tail is not produced by the secondary (as it necessarily is for the BH–NS binary) but likely by the spin-up of the primary. Indeed, the tidal disruption of the secondary, when it still retains a large fraction of its angular momentum, torques and rapidly spins-up the primary, resulting in an extended tidal tail, which, unlike what happens in the equal-mass case, transfers angular momentum outwards very efficiently. This behaviour was first noted by Rezzolla et al. (2010) in the dynamics of unequal-mass binaries described by simple EOSs (see also Sec. 12.5.3 of Rezzolla & Zanotti 2013) and explains why it is naturally absent in BH–NS mergers: such systems contain only one NS, which can only account for one arm of mass ejection. In contrast, NS–NS systems will naturally have two tidal arms, which will become increasingly more asymmetric as the mass ratio is decreased. Furthermore, the most massive of the two tidal arms is the one generated by the disruption of the lightest star in the binary system. In the limit of large mass asymmetries, e.g., $q^{-1} \rightarrow 2$, the heavier of the tidal arm becomes more and more massive until it resembles the tidal arm in a BH–NS merger. At the same time, the lighter tidal arm becomes less massive, but does not disappear even in the limit of the maximum-mass ratio allowed by the maximum mass of the EOS.

In summary, the formation of a double tidal-arm structure is a unique feature of NS–NS mergers, distin-

guishing them from corresponding BH–NS mergers with comparable mass, and is intrinsically associated with the presence of a second NS in the system. As we will discuss in detail below, the low-mass tidal arm from the secondary is composed of matter that is ejected at substantially large velocities, i.e., it can be considered as being mostly made of “fast ejecta” and, for this reason, will have a qualitatively different impact on the electromagnetic counterpart produced in the NS–NS binaries. Note also that because of the large initial mass of the system and the fact that the primary is already close to the critical stability limit to collapse, the merged object almost instantaneously collapses to a BH at merger. In contrast to the case of equal-mass binaries, where the BH properties do not change significantly after its formation, variations in the mass and spin of the BH as large as 5% are possible for unequal-mass systems during the subsequent evolution (Rezzolla et al. 2010).

The overall dynamical picture described above is modified only slightly by the presence of spin in the primary star/BH. A non-zero initial spin will increase the total angular momentum of the merged object and, hence, increase the dynamical ejection of matter. This can be seen in Fig. 3, where we compare the tidal arms in the case of zero spin and low spin, $\tilde{\chi} = 0.15$. We can see that the fast low density arm is, indeed, less massive for low spin cases. In order to assess the dependence on the EOS, the right panels of Fig. 3 show the same simulations performed with the BHBA Φ EOS. The BHBA Φ EOS has a slightly smaller maximum mass but a larger tidal deformability. As a result, the secondary NSs deform more strongly under the tidal field of the primary, lead-

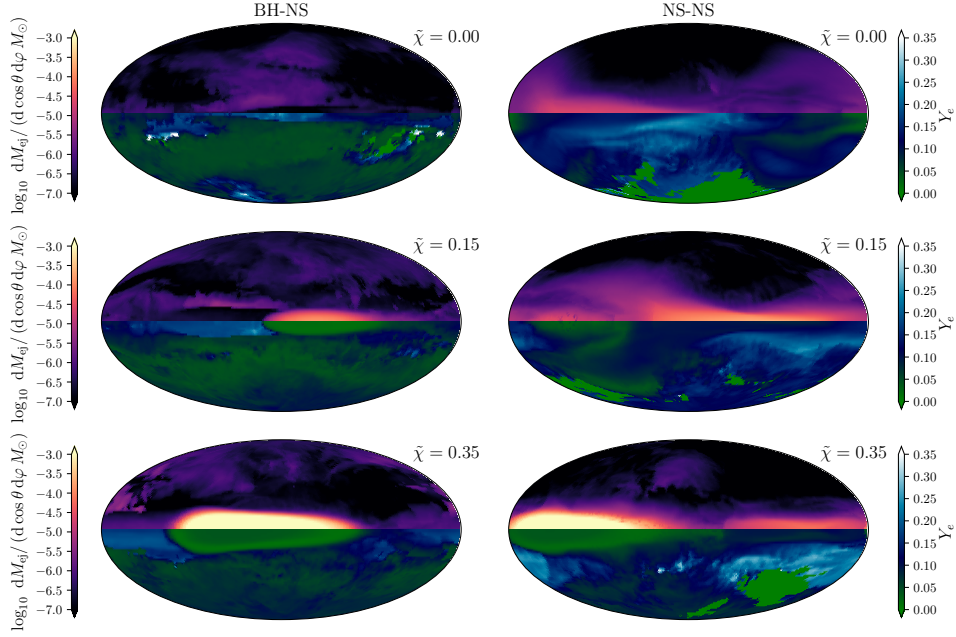


Figure 4. Time-integrated ejected mass M_{ej} and mass-weighted average electron fraction Y_e projected onto a sphere at radius $r = 295$ km from the origin. Shown are the results for NS–NS (left column) and BH–NS mergers (right column) at a time shortly after the two arms have passed the detector. Only unbound fluid elements have been recorded. The rows correspond different effective spins $\tilde{\chi}$. All models have been computed using the TNTYST EOS. We point out that especially at high latitudes where almost no mass is ejected, spurious low density dynamics might lead to artificially high or low Y_e values in those regions. These can safely be ignored as they do not contribute to the overall ejected mass.

ing to an enhanced mass ejection and a larger remnant disk mass in the case of BH–NS merger (Kyutoku et al. 2015; Foucart et al. 2018). On a more qualitative level, we find an increase in mass in the second (fast) arm for the zero spin case (compare left columns of the left and right panels of Fig. 3). In all of the above cases, the main evolution of the tidal tail seems to be almost the same as in the BH–NS case. A detailed analysis and comparison of the properties of the mass ejection will be given in the following.

3.2. Dynamical mass ejection: geometrical and physical distribution

In order to gauge the observational impact of the fast ejecta, we perform a detailed analysis of its properties and composition. We record the mass ejection until the primary (tidal) arm has fully passed the detector (about 5 – 10 ms after merger, see also Fig. 7). In Fig. 4, we start by comparing the final time-integrated angular distributions of the ejecta for the TNTYST EOS simulations when using a Mollweide projection on a spherical surface at a distance of 295 km from the origin. Since the secondary arm is in all cases moving at faster or comparable speeds, it is always fully captured. We only record fluid elements that are unbound according to the Bernoulli criterion, i.e., $hu_t < -1$, where u^μ is the fluid

four-velocity and h the specific fluid enthalpy (Bovard & Rezzolla 2017).

Starting with the zero spin case, $\tilde{\chi} = 0$ (top row), we note that for the BH–NS binary (left column) only very small amounts of ejecta are detected (upper hemispheres) and that the main tidal tail is absent since the system is too bound to tidally eject mass. For the NS–NS binary (right column), the situation is very similar in that the main tidal tail of ejecta is almost absent. However, we also note that the low-mass fast tail is clearly visible as unbound material with a significant proton enhancement, i.e., with $Y_e > 0.1$ (lower hemispheres). While we find that the NS–NS merger can reach temperatures > 100 MeV at the interface between the two stars, the secondary arm is most likely sourced by cold material of the primary NS. Hence, the increased electron fraction is not the result of weak interactions, but corresponds to densities in the outer layers of the primary star that correspond to densities with electron fractions $Y_e > 0.1$ (in beta-equilibrium) (Shen 2002). When increasing the effective spin, $\tilde{\chi} = 0.15$ (middle row), we note that the massive tidal tail becomes unbound and shows up for both BH–NS and NS–NS systems as neutron-rich, i.e., with $Y_e < 0.05$, material ejected mostly along the equatorial plane. In addition to the tidal tail, also the fast ejecta are clearly visible

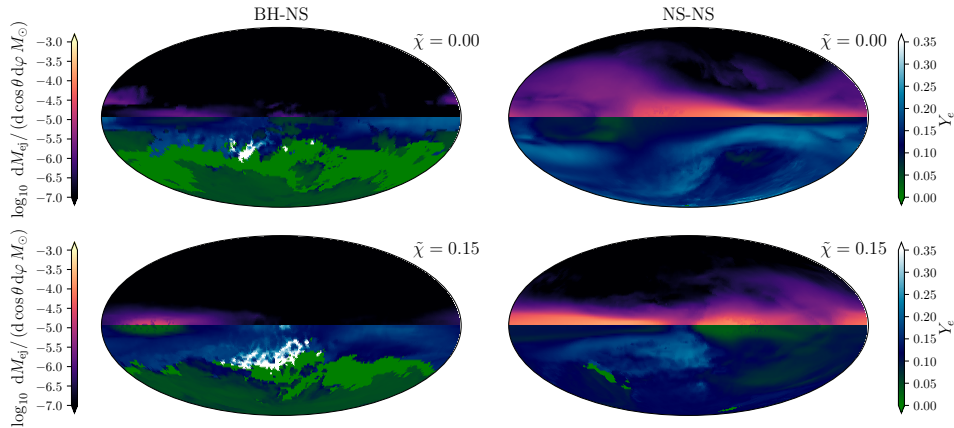


Figure 5. Same as Fig. 4 but for the models using the BHBA Φ EOS.

(and dominant) for the NS–NS system (cf., eastern part of the projection). As for $\tilde{\chi} = 0$, this fast tail does come at higher electron fractions and can be clearly distinguished from the tidal tail, which is ejected in the opposite direction (cf., western part of the projection). Finally, with even higher spin $\tilde{\chi} = 0.35$, the tidal ejection is significantly enhanced as expected from previous studies (Foucart et al. 2014; Kyutoku et al. 2015). The secondary arm is now subdominant but still clearly visible in the NS–NS case.

We contrast these findings with the same results obtained for the stiffer BHBA Φ EOS, which are shown in Fig. 5. While the overall evolution is very similar, for this EOS the mass ejection is enhanced in the case of zero spin in the NS–NS case (top right column). Again, we can clearly distinguish between the two arms by means of the nuclear composition, with the secondary arm having higher electron fractions. Different from the BH–NS case, we find that moderate spins, $\tilde{\chi} = 0.15$, give rise to an increased tidal mass ejection (see the bottom row), although the secondary arm is still the dominant contribution. Overall, the binaries considered here seem to indicate that the amount of tidal ejecta differs between NS–NS and BH–NS binaries having the same mass. We thus conjecture that this difference will mainly depend on the size of the NSs, although follow-up work will be needed to clarify this point. This difference is already present in the apparent sizes of the tidal arms as shown in the right panels of Fig. 3, which are less similar than for the runs with the TNTYST EOS, see Fig. 3.

To complement the information provided so far on the fast tails, we report in Fig. 6 the distribution of the relative mass fraction in terms of the nuclear composition via the electron fraction Y_e (left columns), of the entropy per baryon s (middle columns), and of the

ejecta velocity v (right columns). Different rows refer to different spins, lines of different type but of the same color are representative of either BH–NS (dashed lines) or NS–NS systems (solid lines), while lines of different color but of the same type are representative of binaries evolved with the TNTYST (blue lines) of the BHBA ϕ (red lines) EOS. As anticipated from the angular distribution in Fig. 4, we find that NS–NS systems produce distributions of the electron fraction Y_e that are shifted towards higher values in the low-spin cases. This can be mainly attributed to the appearance of the fast ejecta for NS–NS mergers that dominate the mass ejection. These ejecta come from the outer layers of the primary star, which have higher Y_e values than in the core in beta-equilibrium. More specifically, for simulations with the TNTYST EOS (blue lines), the Y_e distributions peak around $Y_e \simeq 0.15$ (0.10) for spins $\tilde{\chi} = 0.00$ (0.15), with a high Y_e tail in the distribution extending up to $Y_e^{\max} \approx 0.3$ (0.35). In the high-spin case, $\tilde{\chi} = 0.35$, for which we have only simulations with the TNTYST EOS (bottom row), we can also see the appearance of the fast tail in large- Y_e part of the distribution; however, since this ejection is overall subdominant, the bulk peaks of the distributions at $Y_e \lesssim 0.02$ do not shift significantly, as expected for tidal ejecta that are mainly dominated by highly neutron-rich material from the NS core. In this case, the distribution of the fast tail peaks around $Y_e \simeq 0.08$ and extends up to $Y_e < Y_e^{\max} \approx 0.18$. As expected for these type of ejecta they come at very low specific entropies $s < 20 k_B/\text{baryon}$, with the NS–NS distributions having average entropies that are slightly larger than the corresponding ones from BH–NS binaries, as it is obvious given that and actual collision takes place in the first case (see middle column of Fig. 6). Furthermore, the average entropies tend to decrease as the spin in the system is increased, underlining that the

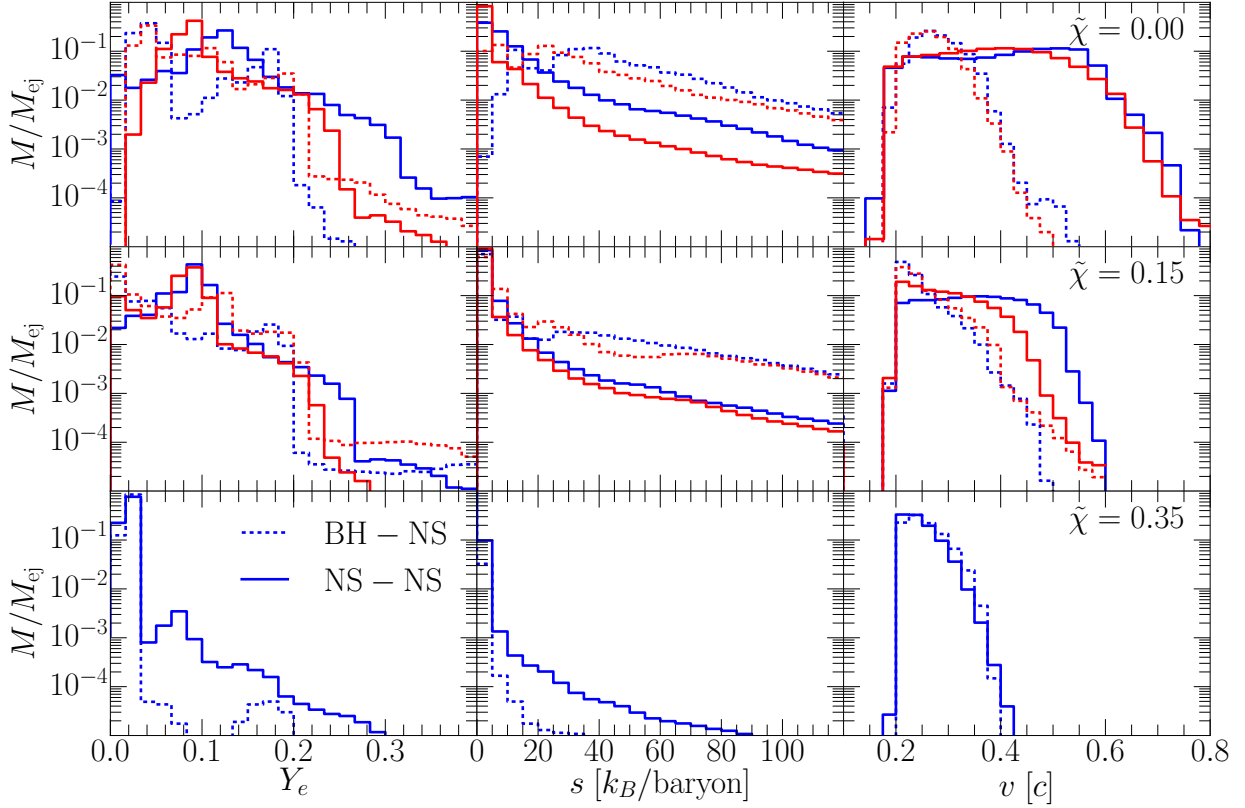


Figure 6. Compositional properties of the dynamical mass ejection. From left to right we show the electron fraction Y_e , the entropy per baryon s and velocity v as computed from the Lorentz factor. Solid lines denote NS–NS and dashed lines BH–NS mergers. The rows correspond to different effective spins $\tilde{\chi}$. Results are shown for the TNTYST (blue) and BH $\Lambda\Phi$ (red) EOSs.

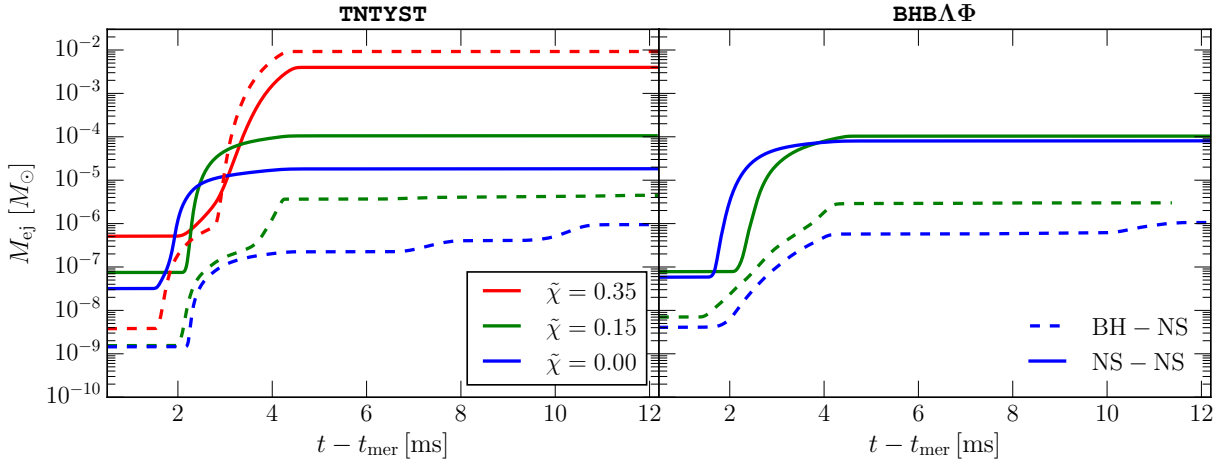


Figure 7. Ejected mass M_{ej} for the different configurations as a function of effective spin $\tilde{\chi}$ relative to the time of merger t_{mer} .

disruption process is less energetic with more rapidly spinning primaries.

Crucially, the existence of a secondary tidal arm in the NS–NS systems gives rise to a velocity distribution that has a large and massive portion with velocities $0.5 \lesssim v \lesssim 0.8$. This can be clearly seen in the top-right panel of Fig. 6. Note also that because these

high-velocity tails are absent in the corresponding BH–NS mergers, they certainly represent the most important difference discriminating BH–NS and NS–NS systems having the same mass. As the spin of the primary is increased, the high-velocity become less pronounced. In fact, the fast-ejecta tails essentially disappear in the $\tilde{\chi} = 0.35$ case, where BH–NS and NS–NS mergers yield

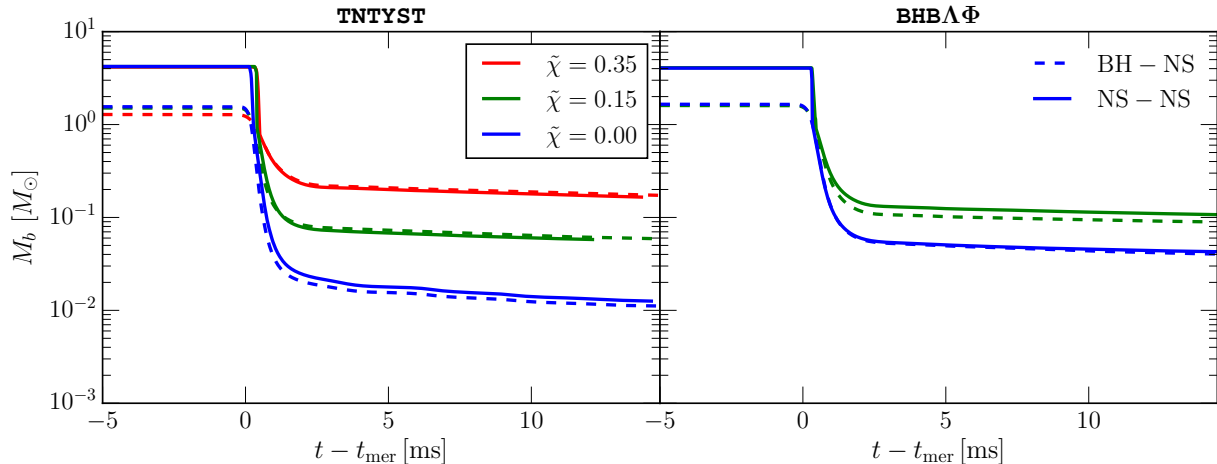


Figure 8. Baryon mass M_b outside of the apparent horizon at any point during the simulation. After the sudden drop at merger, these curves represent the matter inside the accretion disk (outside of the apparent horizon) and in the ejecta. NS–NS mergers are denoted by solid lines, while BH–NS mergers with dashed lines.

overall the same velocity distributions (see bottom right, Fig. 6). Although there is still considerable mass in this secondary tidal arm (see bottom left, Fig. 4), it has the same velocities as the main tidal tail ejecta. This behaviour is easy to interpret: in the $\tilde{\chi} = 0.35$ case, the primary star is already spinning rapidly and a further sudden spin-up through the merger process does not have lead to the ejection of rapidly moving matter.

So far, the previous discussion only weakly depends on the EOS and, overall, evolutions with the BHBA Φ EOS (red lines) give very similar distributions, with the minor difference that the distributions cut-off earlier at high Y_e and for the zero-spin case are shifted to slightly lower electron fractions, i.e., $Y_e \simeq 0.1$.

It should be remarked that the fast ejecta are produced over a very short window in time around the merger. This is clearly summarized in Fig. 7, which reports the evolution of ejected rest-mass M_{ej} for the different configurations as a function of effective spin $\tilde{\chi}$ relative to the time of merger t_{mer} . Note that the spin in the primary is responsible for a considerable amplification of the amount of ejected mass (cf., the $\tilde{\chi} = 0$ and $\tilde{\chi} = 0.35$ cases). While this is more severe for BH–NS systems – where the amplification is of about four orders of magnitude – the ejected mass can grow by a factor $\lesssim 100$ in the case of NS–NS systems.

Furthermore, because of the rapidity with which mass is ejected, the amount of mass that is present in the disk around the newly formed BH will not differ significantly between the BH–NS and the NS–NS binaries considered here. This is shown in Fig. 8, which reports the baryon mass M_b outside of the apparent horizon at any point during the simulation; here too, different lines refer to either BH–NS mergers (dashed lines) or to NS–NS mergers

(solid lines). After the sudden drop at merger, these curves essentially represent the combined matter inside the accretion disk as well as in the ejecta. By comparing the remnant baryon masses after the merger for the various binaries it is apparent that the disks formed in both mergers are essentially the same and that the fast ejecta constitute only a small fraction of the total baryonic mass outside the BH. We summarize this in Table 2, which collects the properties of the ejected and bound mass after the merger for the various binaries considered. Remarkably, all mergers with different spins and different EOSs yield comparable amounts of baryon mass for BH–NS and NS–NS systems, which are in good agreement with previous estimates (Foucart et al. 2018).

As a concluding remark, we discuss the prospects that these fast ejecta may actually be detectable and leave an imprint that is different from the standard afterglow emission coming from the disk winds of the remnant accretion disk (Fernández et al. 2015a,b; Siegel & Metzger 2017). Since both systems start out with the same gravitational masses and spins, the final spacetime after merger, i.e., the properties of the final BH, will be very similar in both cases. As the main differences in the disk ejection can only be driven by different properties of the accretion disks and these do not vary significantly across the binaries considered (cf., Fig. 8), the afterglow emission coming from the disk winds should be comparable in both cases. Hence, the most visible impact that the fast ejecta may potentially leave is in the kilonova emission, whose modelling needs to take into account the (asymptotic) ejecta velocity achieved in the homologous-expansion phase and which obviously depends on the velocity at the ejecting site (see discussion in Bovard et al. 2017). Indeed, the fast ejecta launched at merger could

Table 2. Properties of the ejected and bound mass after the merger. Shown are the values of the ejected baryon mass for BH–NS and for NS–NS mergers. In the latter case, we also give the mass of the ejecta having speeds $v > 0.4$, $M_{\text{ej}}^{\text{fast}}$, and the kinetic energy, T_{ej} . We finally report the remnant baryon mass, M_b^{fin} , that has not been accreted by the end of the simulation and contrast it with the analytic estimate M_b^{FHN} of Foucart et al. (2018).

	$M_{\text{ej}} [M_{\odot}]$	$M_{\text{ej}}^{\text{fast}} [M_{\odot}]$	$T_{\text{ej}} [\text{erg}]$	$M_b^{\text{fin}} [M_{\odot}]$	$M_b^{\text{FHN}} [M_{\odot}]$	$\tilde{\chi}$
TNT.BH.chit.0.00	9.5×10^{-7}	1.6×10^{-9}	4.3×10^{48}	1.3×10^{-2}	6.4×10^{-3}	0.00
TNT.BH.chit.0.15	4.5×10^{-6}	1.1×10^{-8}	1.6×10^{49}	5.8×10^{-2}	5.1×10^{-2}	0.15
TNT.BH.chit.0.35	9.2×10^{-3}	1.4×10^{-8}	3.0×10^{50}	1.7×10^{-1}	1.8×10^{-1}	0.35
TNT.NS.chit.0.00	1.8×10^{-5}	1.1×10^{-5}	1.0×10^{47}	1.1×10^{-2}	–	0.00
TNT.NS.chit.0.15	1.1×10^{-4}	3.2×10^{-5}	3.6×10^{47}	5.4×10^{-2}	–	0.15
TNT.NS.chit.0.35	4.0×10^{-3}	3.4×10^{-7}	7.6×10^{50}	1.5×10^{-1}	–	0.35
BHBLP.BH.chit.0.00	1.1×10^{-6}	1.1×10^{-9}	1.0×10^{47}	3.3×10^{-2}	3.6×10^{-2}	0.00
BHBLP.BH.chit.0.15	3.0×10^{-6}	8.7×10^{-9}	2.5×10^{47}	7.3×10^{-2}	1.0×10^{-1}	0.15
BHBLP.NS.chit.0.00	7.9×10^{-5}	3.9×10^{-5}	2.8×10^{48}	3.5×10^{-2}	–	0.00
BHBLP.NS.chit.0.15	1.0×10^{-4}	6.3×10^{-6}	1.1×10^{49}	8.7×10^{-2}	–	0.15

lead to a bright kilonova precursors just hours after the merger (Metzger et al. 2015), or to a synchrotron emission several years later (Hotokezaka et al. 2018). We will comment on this further in the next section.

4. DISCUSSION

We have explored and contrasted the dynamics of binary NS–NS and BH–NS mergers that could be representative of high-mass gravitational-wave events such as GW190425 (Abbott et al. 2020). By choosing total masses and mass ratios such that the primary mass m_1 is close to the maximum mass of nonrotating NSs, we were able to investigate a region of the space of parameters where a realistic overlap between the two scenarios exists. By performing fully general-relativistic magnetohydrodynamics simulations of the merger of the two types of binary systems, we were able to show that the main mass ejection mechanism through the secondary, as well as the remnant disk mass is comparable in both cases.

While this indicates that the kilonova emission expected for these systems (Fernández et al. 2015a,b; Siegel & Metzger 2017), is likely going to be very similar, we identified another mass-ejection channel that could help to distinguish a primary NS from a primary BH in the two binary systems. More specifically, we found that in a NS–NS system the presence of a massive NS and the consequent spin-up at merger through the torques exerted by the secondary leads to a second burst of mass ejection propagating in the direction opposite to that of the main tidal tail. By carefully analysing the matter properties in terms of its geometrical and physical distributions, we were able to show that the second

mass-ejection burst is propagating at very high speeds, $0.5 \lesssim v \lesssim 0.8$ for irrotational binaries. This is considerably larger than for a BH–NS system with the same mass, whose velocity distribution is $v \lesssim 0.5$, when comparing the second tidal arm produced by the spin-up of the primary star with the first tidal arm produced by the disruption of the secondary star, we have shown that the former is also considerably more proton rich, with a peak in the distributions at $Y_e \approx 0.12$. Hence, these high-velocity tidal certainly represent the most important difference discriminating BH–NS and NS–NS systems having the same (high) mass.

It has been proposed that such fast dynamical ejecta produced at merger can lead to bright kilonova precursors just hours after the merger (Metzger et al. 2015), or to a synchrotron emission several years later (Hotokezaka et al. 2018). However, so far searches for this X-ray re-brightening in the afterglow of GW170817 have remained inconclusive (Troja et al. 2020). In particular, in the case of a precursor to the kilonova afterglow, Metzger et al. (2015) found that for optimistic estimates of the opacity, an amount of ejecta of $\sim 3 \times 10^{-5} M_{\odot}$, are sufficient to produce a beta-decay powered reheating of the afterglow, which would lead to a luminosity peak at ~ 1 hour after the merger. While this matches well with our results, we caution that because the fast ejecta we have found in the NS–NS systems are less neutron rich, this will result in a reduced availability of free neutrons to undergo beta-decay. Additionally, the strong concentration of these ejecta along the equatorial plane would also reduce the detectability prospects, especially for a transient that would only be visible in the first few hours

after merger (Metzger et al. 2015). On the other hand, if the interaction of the fast ejecta with the interstellar medium would indeed produce a re-brightening of the afterglow (Hotokezaka et al. 2018), we estimate that even in the most optimistic case, i.e., BHBL.chit.0.15, a radio peak flux of $F_\nu \lesssim 1 \mu\text{Jy}$ (at 3 GHz), which would likely not be detectable (see Sec. 5.1 of Radice et al. 2018, for details).

Besides the present objective difficulties in observing the presence of these fast ejecta, we should also comment on the limitations of our numerical study. By its very nature, tidal disruption crucially depends on the radius of the NS. It has been shown that large stars, which are affected more strongly by tidal forces, feature enhanced mass ejection (Foucart et al. 2013; Kyutoku et al. 2015; Foucart et al. 2018). To address this we have chosen only two EOSs spanning the range of radii compatible with GW170817 (Most et al. 2018), without fully exploring it. These two EOS naturally come with fixed maximum masses that are not far apart. In particular, should the maximum mass be much higher than $M_{\text{TOV}} \gg 2.3 M_\odot$ (Tan et al. 2020; Fattoyev et al. 2020), a regime of even higher mass ratios should also be explored.

Finally, for obvious computational costs, we have limited ourselves to only a single total mass, $M_{\text{tot}} = 3.6 M_\odot$, restricting the mass ratio, the mass and spin of the secondary. Future work will be needed to elucidate this dependence, in particular with respect to the

fast tail of the mass ejection for NS–NS mergers. Such a study will need to be accompanied by a careful (re-)analysis of lower mass NS–NS systems, in order to understand the maximum mass ratio at which fast ejecta along the equatorial plane are to be expected (Bernuzzi et al. 2020).

ACKNOWLEDGEMENTS

ERM thanks Carolyn Raithel for insightful discussions on neutron-star composition. ERM gratefully acknowledges support from a joint fellowship at the Princeton Center for Theoretical Science, the Princeton Gravity Initiative and the Institute for Advanced Study. The simulations were performed on the national supercomputer HPE Apollo Hawk at the High Performance Computing Center Stuttgart (HLRS) under the grant number BBHDISKS. The authors gratefully acknowledge the Gauss Centre for Supercomputing e.V. (www.gauss-centre.eu) for funding this project by providing computing time on the GCS Supercomputer SuperMUC at Leibniz Supercomputing Centre (www.lrz.de). LR gratefully acknowledges funding from HGS-HIRE for FAIR; the LOEWE-Program in HIC for FAIR; “PHAROS”, COST Action CA16214.

Software: Einstein Toolkit (Loeffler et al. 2012), Carpet (Schnetter et al. 2004), AHFinderDirect (Thornburg 2004), Frankfurt-/IllinoisGRMHD (FIL) (Most et al. 2019b; Etienne et al. 2015), LORENE (https://lorene.obspm.fr), Kadath(Grandclement 2010)

REFERENCES

- Abbott, B. P., Abbott, R., Abbott, T. D., et al. 2017, *Phys. Rev. Lett.*, **119**, 161101
- . 2018, *Physical Review Letters*, **121**, 161101
- . 2020, *Astrophys. J. Lett.*, **892**, L3
- Ackley, K., Amati, L., Barbieri, C., et al. 2020, arXiv e-prints, arXiv:2002.01950
- Alic, D., Bona-Casas, C., Bona, C., Rezzolla, L., & Palenzuela, C. 2012, *Phys. Rev. D*, **85**, 064040
- Alsing, J., Silva, H. O., & Berti, E. 2018, *Mon. Not. R. Astron. Soc.*, **478**, 1377
- Andreoni, I., Goldstein, D. A., Kasliwal, M. M., et al. 2020, *Astrophys. J.*, **890**, 131
- Annala, E., Ecker, C., Hoyos, C., et al. 2018, *Journal of High Energy Physics*, **2018**, 78
- Antoniadis, J., Freire, P. C. C., Wex, N., et al. 2013, *Science*, **340**, 448
- Baiotti, L., Giacomazzo, B., & Rezzolla, L. 2008, *Phys. Rev. D*, **78**, 084033
- Banik, S., Hempel, M., & Bandyopadhyay, D. 2014, *Astrophys. J. Suppl.*, **214**, 22
- Bernuzzi, S., & Hilditch, D. 2010, *Phys. Rev. D*, **81**, 084003
- Bernuzzi, S., Breschi, M., Daszuta, B., et al. 2020, arXiv e-prints, arXiv:2003.06015
- Biswas, B., Nandi, R., Char, P., Bose, S., & Stergioulas, N. 2020, arXiv e-prints, arXiv:2010.02090
- Bovard, L., Martin, D., Guercilena, F., et al. 2017, *Phys. Rev. D*, **96**, 124005
- Bovard, L., & Rezzolla, L. 2017, *Classical and Quantum Gravity*, **34**, 215005
- Breu, C., & Rezzolla, L. 2016, *Mon. Not. R. Astron. Soc.*, **459**, 646
- Cao, Z., Chen, L.-W., Chu, P.-C., & Zhou, Y. 2020, arXiv e-prints, arXiv:2009.00942
- Caudill, M., Cook, G. B., Grigsby, J. D., & Pfeiffer, H. P. 2006, *Phys. Rev. D*, **74**, 064011
- Coughlin, M. W., Dietrich, T., Antier, S., et al. 2020, *Mon. Not. R. Astron. Soc.*, **492**, 863

- Cromartie, H. T., Fonseca, E., Ransom, S. M., et al. 2020, *Nature Astronomy*, 4, 72
- De, S., Finstad, D., Lattimer, J. M., et al. 2018, *Physical Review Letters*, 121, 091102
- Del Zanna, L., Zanotti, O., Bucciantini, N., & Londrillo, P. 2007, *Astron. Astrophys.*, 473, 11
- Dexheimer, V., Gomes, R. O., Klähn, T., Han, S., & Salinas, M. 2020, arXiv e-prints, arXiv:2007.08493
- Dietrich, T., Ujevic, M., Tichy, W., Bernuzzi, S., & Brüggmann, B. 2017, *Phys. Rev. D*, 95, 024029
- Dionysopoulou, K., Alic, D., & Rezzolla, L. 2015, *Phys. Rev. D*, 92, 084064
- Dobie, D., Stewart, A., Murphy, T., et al. 2019, *Astrophys. J. Lett.*, 887, L13
- Duez, M. D., Liu, Y. T., Shapiro, S. L., & Stephens, B. C. 2005, *Phys. Rev. D*, 72, 024028
- Ertl, T., Woosley, S. E., Sukhbold, T., & Janka, H. T. 2020, *Astrophys. J.*, 890, 51
- Essick, R., & Landry, P. 2020, arXiv e-prints, arXiv:2007.01372
- Etienne, Z. B., Faber, J. A., Liu, Y. T., Shapiro, S. L., & Baumgarte, T. W. 2007, *Phys. Rev. D*, 76, 101503
- Etienne, Z. B., Liu, Y. T., Shapiro, S. L., & Baumgarte, T. W. 2009, *Phys. Rev. D*, 79, 044024
- Etienne, Z. B., Paschalidis, V., Haas, R., Mösta, P., & Shapiro, S. L. 2015, *Class. Quantum Grav.*, 32, 175009
- Falcke, H., & Rezzolla, L. 2014, *Astron. Astrophys.*, 562, A137
- Fattouev, F. J., Horowitz, C. J., Piekarewicz, J., & Reed, B. 2020, arXiv e-prints, arXiv:2007.03799
- Fernández, R., Kasen, D., Metzger, B. D., & Quataert, E. 2015a, *Mon. Not. R. Astron. Soc.*, 446, 750
- Fernández, R., Quataert, E., Schwab, J., Kasen, D., & Rosswog, S. 2015b, *Mon. Not. R. Astron. Soc.*, 449, 390
- Foley, R. J., Coulter, D. A., Kilpatrick, C. D., et al. 2020, *Mon. Not. R. Astron. Soc.*, 494, 190
- Foucart, F. 2012, *Phys. Rev. D*, 86, 124007
- Foucart, F., Duez, M. D., Kidder, L. E., et al. 2019, *Phys. Rev. D*, 99, 103025
- . 2012, *Phys. Rev. D*, 85, 044015
- Foucart, F., Hinderer, T., & Nissanke, S. 2018, *Phys. Rev. D*, 98, 081501
- Foucart, F., Deaton, M. B., Duez, M. D., et al. 2013, *Phys. Rev. D*, 87, 084006
- . 2014, *Phys. Rev. D*, 90, 024026
- Foucart, F., Haas, R., Duez, M. D., et al. 2016, *Phys. Rev. D*, 93, 044019
- Fryer, C. L., Rueda, J. A., & Ruffini, R. 2014, *Astrophys. J. Lett.*, 793, L36
- Fujibayashi, S., Sekiguchi, Y., Kiuchi, K., & Shibata, M. 2017, *Astrophys. J.*, 846, 114
- Galeazzi, F., Kastaun, W., Rezzolla, L., & Font, J. A. 2013, *Phys. Rev. D*, 88, 064009
- García-Bellido, J., Linde, A., & Wands, D. 1996, *Phys. Rev. D*, 54, 6040
- Giacomazzo, B., & Rezzolla, L. 2007, *Class. Quantum Grav.*, 24, 235
- Giacomazzo, B., Rezzolla, L., & Baiotti, L. 2011, *Phys. Rev. D*, 83, 044014
- Godzieba, D. A., Radice, D., & Bernuzzi, S. 2020, arXiv e-prints, arXiv:2007.10999
- Grandclément, P. 2006, *Phys. Rev. D*, 74, 124002
- Grandclément, P. 2010, *J. Comput. Phys.*, 229, 3334
- Hamers, A. S., & Safarzadeh, M. 2020, *Astrophys. J.*, 898, 99
- Harry, I., & Hinderer, T. 2018, *Classical and Quantum Gravity*, 35, 145010
- Hayashi, K., Kawaguchi, K., Kiuchi, K., Kyutoku, K., & Shibata, M. 2020, arXiv e-prints, arXiv:2010.02563
- Hempel, M., & Schaffner-Bielich, J. 2010, *Nuclear Physics A*, 837, 210
- Hilditch, D. 2013, *International Journal of Modern Physics A*, 28, 1340015
- Hinderer, T., Nissanke, S., Foucart, F., et al. 2019, *Phys. Rev. D*, 100, 063021
- Hotokezaka, K., Kiuchi, K., Shibata, M., Nakar, E., & Piran, T. 2018, *Astrophys. J.*, 867, 95
- Izzo, L., Rueda, J. A., & Ruffini, R. 2012, *Astron. & Astrophys.*, 548, L5
- Kawaguchi, K., Shibata, M., & Tanaka, M. 2020, *Astrophys. J.*, 893, 153
- Kruckow, M. U., Tauris, T. M., Langer, N., Kramer, M., & Izzard, R. G. 2018, *Mon. Not. R. Astron. Soc.*, 481, 1908
- Kyutoku, K., Fujibayashi, S., Hayashi, K., et al. 2020, arXiv e-prints, arXiv:2001.04474
- Kyutoku, K., Ioka, K., Okawa, H., Shibata, M., & Taniguchi, K. 2015, *Phys. Rev. D*, 92, 044028
- Kyutoku, K., Ioka, K., & Shibata, M. 2013, *Phys. Rev. D*, 88, 041503
- Kyutoku, K., Kiuchi, K., Sekiguchi, Y., Shibata, M., & Taniguchi, K. 2018, *Phys. Rev. D*, 97, 023009
- Kyutoku, K., Okawa, H., Shibata, M., & Taniguchi, K. 2011, *Phys. Rev. D*, 84, 064018
- Lehner, L., Liebling, S. L., Palenzuela, C., et al. 2016, *Classical and Quantum Gravity*, 33, 184002
- Lim, Y., Bhattacharya, A., Holt, J. W., & Pati, D. 2020, arXiv e-prints, arXiv:2007.06526
- Liu, B., & Lai, D. 2020, arXiv e-prints, arXiv:2009.10068

- Loeffler, F., Faber, J., Bentivegna, E., et al. 2012, *Class. Quantum Grav.*, **29**, 115001
- Lu, W., Beniamini, P., & Bonnerot, C. 2020, arXiv e-prints, arXiv:2009.10082
- Mandel, I., Mueller, B., Riley, J., et al. 2020, arXiv e-prints, arXiv:2007.03890
- Margalit, B., & Metzger, B. D. 2017, *Astrophys. J. Lett.*, **850**, L19
- Metzger, B. D. 2017, *Living Reviews in Relativity*, **20**, 3
- Metzger, B. D., Bauswein, A., Goriely, S., & Kasen, D. 2015, *Mon. Not. R. Astron. Soc.*, **446**, 1115
- Miller, J. M., Ryan, B. R., Dolence, J. C., et al. 2019, *Phys. Rev. D*, **100**, 023008
- Most, E. R., Papenfort, L. J., Dexheimer, V., et al. 2019a, *Physical Review Letters*, **122**, 061101
- Most, E. R., Papenfort, L. J., & Rezzolla, L. 2019b, *Mon. Not. R. Astron. Soc.*, **490**, 3588
- Most, E. R., Papenfort, L. J., Weih, L. R., & Rezzolla, L. 2020a, arXiv e-prints, arXiv:2006.14601
- Most, E. R., Weih, L. R., & Rezzolla, L. 2020b, *Mon. Not. R. Astron. Soc.*, **496**, L16
- Most, E. R., Weih, L. R., Rezzolla, L., & Schaffner-Bielich, J. 2018, *Phys. Rev. Lett.*, **120**, 261103
- Papenfort, L. J., Tootle, S., Grandclement, P., Most, E. R., & Rezzolla, L. 2020, in preparation, arXiv:in preparation
- Perego, A., Cabezón, R. M., & Käppeli, R. 2016, *The Astrophysical Journal Supplement Series*, **223**, 22
- Pfeiffer, H. P., & York, J. W. 2003, *Phys. Rev. D*, **67**, 044022
- Pfeiffer, H. P., & York, J. W. 2005, *Phys. Rev. Lett.*, **95**, 091101
- Qin, B., Wu, X.-P., Chu, M.-C., Fang, L.-Z., & Hu, J.-Y. 1998, *The Astrophysical Journal*, **494**, L57
- Radice, D., Perego, A., Hotokezaka, K., et al. 2018, *Astrophys. J.*, **869**, 130
- Rezzolla, L., Baiotti, L., Giacomazzo, B., Link, D., & Font, J. A. 2010, *Class. Quantum Grav.*, **27**, 114105
- Rezzolla, L., Most, E. R., & Weih, L. R. 2018, *Astrophys. J. Lett.*, **852**, L25
- Rezzolla, L., & Zanotti, O. 2013, *Relativistic Hydrodynamics* (Oxford, UK: Oxford University Press)
- Rosswog, S. 2005, *Astrophys. J.*, **634**, 1202
- Rosswog, S., & Liebendörfer, M. 2003, *Mon. Not. R. Astron. Soc.*, **342**, 673
- Roupas, Z. 2020, arXiv e-prints, arXiv:2007.10679
- Rueda, J. A., & Ruffini, R. 2012, *Astrophys. J. Lett.*, **758**, L7
- Ruffert, M., Janka, H.-T., & Schaefer, G. 1996, *Astron. Astrophys.*, **311**, 532
- Ruiz, M., Shapiro, S. L., & Tsokaros, A. 2018, *Phys. Rev. D*, **97**, 021501
- Safarzadeh, M., & Loeb, A. 2020, arXiv e-prints, arXiv:2007.00847
- Schnetter, E., Hawley, S. H., & Hawke, I. 2004, *Class. Quantum Grav.*, **21**, 1465
- Sedrakian, A., Weber, F., & LI, J.-J. 2020, arXiv e-prints, arXiv:2007.09683
- Sekiguchi, Y., Kiuchi, K., Kyutoku, K., & Shibata, M. 2015, *Phys. Rev. D*, **91**, 064059
- Shen, H. 2002, *Phys. Rev. C*, **65**, 035802
- Shibata, M., & Sekiguchi, Y.-I. 2005, *Phys. Rev. D*, **72**, 044014
- Shibata, M., & Taniguchi, K. 2011, *Living Rev. Relativity*, **14**
- Shibata, M., Zhou, E., Kiuchi, K., & Fujibayashi, S. 2019, *Phys. Rev. D*, **100**, 023015
- Siegel, D. M., & Metzger, B. D. 2017, *Physical Review Letters*, **119**, 231102
- Suwa, Y., Yoshida, T., Shibata, M., Umeda, H., & Takahashi, K. 2018, *Mon. Not. R. Astron. Soc.*, **481**, 3305
- Tacik, N., Foucart, F., Pfeiffer, H. P., et al. 2015, *Phys. Rev. D*, **92**, 124012
- Tan, H., Noronha-Hostler, J., & Yunes, N. 2020, arXiv e-prints, arXiv:2006.16296
- Taniguchi, K., Baumgarte, T. W., Faber, J. A., & Shapiro, S. L. 2005, *Phys. Rev. D*, **72**, 044008
- . 2007, *Phys. Rev. D*, **75**, 084005
- Tauris, T. M., Kramer, M., Freire, P. C. C., et al. 2017, *Astrophys. J.*, **846**, 170
- Tews, I., Pang, P. T. H., Dietrich, T., et al. 2020, arXiv e-prints, arXiv:2007.06057
- The LIGO Scientific Collaboration, the Virgo Collaboration, Abbott, B. P., et al. 2017, *Astrophys. J. Lett.*, **848**, L12
- The LIGO Scientific Collaboration, the Virgo Collaboration, Abbott, R., et al. 2020, *Astrophys. J. Lett.*, **896**, L44
- Thornburg, J. 2004, *Class. Quantum Grav.*, **21**, 743
- Tichy, W. 2012, *Phys. Rev. D*, **86**, 064024
- Togashi, H., Nakazato, K., Takehara, Y., et al. 2017, *Nucl. Phys.*, **A961**, 78
- Troja, E., van Eerten, H., Zhang, B., et al. 2020, *Mon. Not. R. Astron. Soc.*, **498**, 5643
- Tsokaros, A., Ruiz, M., & Shapiro, S. L. 2020, arXiv e-prints, arXiv:2007.05526
- Tsokaros, A., Uryū, K., & Rezzolla, L. 2015, *Phys. Rev. D*, **91**, 104030
- Vattis, K., Goldstein, I. S., & Koushiappas, S. M. 2020, *Phys. Rev. D*, **102**, 061301

- Vieira, N., Ruan, J. J., Haggard, D., et al. 2020, *Astrophys. J.*, 895, 96
- Watson, A. M., Butler, N. R., Lee, W. H., et al. 2020, *Mon. Not. R. Astron. Soc.*, 492, 5916
- Zdziarski, A. A., Mikolajewska, J., & Belczynski, K. 2013, *Mon. Not. R. Astron. Soc.*, 429, L104
- Zevin, M., Spera, M., Berry, C. P. L., & Kalogera, V. 2020, arXiv e-prints, arXiv:2006.14573
- Zhang, N.-B., & Li, B.-A. 2020, arXiv e-prints, arXiv:2007.02513